Acta Materialia 182 (2020) 215–225

Contents lists available at ScienceDirect

Acta Materialia

journal homepage: www.elsevier.com/locate/actamat

Full length article

Tailoring ultra-strong nanocrystalline tungsten nanofoams by reverse phase dissolution

Mingyue Zhao[a,*], Inas Issa[a], Manuel J. Pfeifenberger[b], Michael Wurmshuber[a], Daniel Kiener[a]

[a] Chair of Materials Physics, Montanuniversität Leoben, Jahnstraße 12, 8700 Leoben, Austria
[b] Erich Schmid Institute of Materials Science, Austrian Academy of Sciences, Jahnstraße 12, 8700 Leoben, Austria

ARTICLE INFO

Article history:
Received 19 June 2019
Revised 10 October 2019
Accepted 11 October 2019
Available online 30 October 2019

Keywords:
Nanoporous tungsten
Selective phase dissolution
Microstructure characterization
Nanoindentation

ABSTRACT

Bulk nanoporous tungsten as an extremely strong and low density nanocrystalline material was for the first time created to satisfy the need for advanced high performance materials that can endure harsh environments. Synthesis of nanoporous tungsten was achieved by a unique procedure involving severe plastic deformation of a coarse-grained tungsten-copper composite followed by selective dissolution of the nobler copper phase. The used ammonium persulfate etching solution, in which the less noble tungsten is chemically stable, is proved to be effective in removing the nobler copper phase. A nanoporous microstructure characterized by a network of interconnected nanocrystalline tungsten ligaments and interconnected nanopores was obtained. Based on a high-resolution interface analysis, the underlined mechanisms for formation of the nanoporous tungsten structure were elucidated. Moreover, using nanoindentation we demonstrate that, due to the nanoscale microstructure, the created nanoporous tungsten possesses outstanding strength, making it an attractive material for applications in radiation shielding.

1. Introduction

Tungsten (W) and W alloys are commonly applied as radiation shielding materials in nuclear facilities [1], medical diagnosis systems [2], particle accelerators [3,4], and many other circumstances to protect personnel and sensitive equipment from radiation. In industrial projects, there are two main types of radiation requiring shielding materials: (i) X and gamma-rays radiation; (ii) neutron radiation. W and W alloys can effectively attenuate or absorb ionizing X- and gamma-rays radiation as W has a high atomic number (Z) [5]. But in the neutron attenuation applications, their performance is quite ineffective, as the neutrons are uncharged and can simply pass through them. On the contrary, materials composed of low Z elements, such as the compounds of hydrogen and boron, are preferable for stopping this type of radiation because they have a higher probability of forming cross-section that will interact with the neutrons through elastic scattering. However, the materials composed of low Z elements can emit gamma-rays when blocking neutrons, meaning that neutron radiation shielding is most effective when it incorporates both high and low Z element [6].

W materials are presently considered as top candidates for plasma-facing armor or shield component and as structural component in DEMO designs due to their mechanical strength, high melting point, good thermal conductivity, high sputter threshold, and low sputtering yield [7]. For these applications, tungsten will be exposed to high doses of low energy helium and neutron radiation of approximately hundreds of dpa for an anticipated 3–5 year lifetime [8,9], which leads to radiation damage denoted by the formation of interstitial loops, dislocations, vacancy clusters, helium bubbles and cavities [10,11]. The radiation damage alters the mechanical properties [12,13] of the material and changes its microstructure [14–16]. The detrimental changes in mechanical properties such as swelling [12], embrittlement [17] and hardening [18] can lead to failure of the components [12]. In

Abbreviations: W, tungsten; GB, grain boundary; np, nanoporous; SPD, severe plastic deformation; HPT, high pressure torsion; nc, nanocrystalline; 3D, three-dimensional; $(NH_4)_2S_2O_8$, ammonium persulfate; WO_3, tungsten oxides; NaOH, sodium hydroxide; SEM, scanning electron microscope; EDX, energy dispersive X-ray spectrometer; FIB, focused ion beam; TEM, transmission electron microscope; BF, bright field; HR, high resolution; STEM, scanning transmission electron microscope; SAED, selected area electron diffraction; FFT, fast Fourier transform; HAADF, high-angle annular dark field; PB, phase boundary; CSM, continuous stiffness measurement.

* Corresponding author.
E-mail address: mingyue.zhao@unileoben.ac.at (M. Zhao).

https://doi.org/10.1016/j.actamat.2019.10.030

order to extend the life time of current nuclear reactors and to develop next generation nuclear reactors, it is essential to discover novel materials or to alter the existing materials that resist the microstructural damage and the consequent mechanical properties degradation when exposed to extreme neutron or ion particle irradiation [12].

Metallic foams (i.e. porous metals) are materials with the potential to show radiation resistance as the free surfaces are perfect sinks for radiation-induced point defects. In the case of nuclear fuels, which develop a natural foam-forming tendency due to fission gas accumulation, the idea of starting with a porous structure to accommodate the gas has been proposed for advanced fuels [19]. Metallic foams possess also a number of other positive attributes such as low density, large surface area and excellent thermal properties [20]. These properties render them as promising candidates to be studied as future radiation shielding materials. In general, there are three different types of metallic foams: open cell, closed cell, or a combination of the two [21]. The open-cell foam, comprising of a network of interconnected solid ligaments and interconnected pores, allows the continuous penetration of the gas or fluid media. By infiltrating the empty pores with hydrogen or boron compounds, these open-cell metallic foams would possess excellent radiation shielding capability in thermal neutron attenuation experiments as well [22]. However, common open-cell metallic foams (ligament size $>>$ 500 nm) cannot meet the requirements for their use as radiation-resistant materials especially in such extreme environments as nuclear reactors, as their ligaments behave as bulk materials and tend to accumulate damage, and their stiffness and strength governed by cell wall bending for all loading conditions is comparatively low [23].

Nanostructuring has long been known as a useful ductilization and toughening strategy for W plasma-facing armor and structural materials, as the yield strength significantly increases due to grain size refinement [1,24,25]. Meanwhile, radiation-induced embrittlement is mitigated by nanostructures that contain a high density of sinks, such as grain boundaries (GBs) and free surfaces, so as to annihilate radiation-induced point defects [26] and to trap He [27]. Metallic foams with grains and pores at the nanoscale, i.e. nanofoams, are therefore expected to exhibit excellent mechanical properties and superior irradiation endurance, as they have an extremely large amount of interfaces including GBs and free surfaces.

The integration of computer simulations and experiments on model np Au films [28] show that, for a given temperature, there exists a window in the foam parameter space of radiation dose versus ligament size where such materials would show radiation tolerance. The borders to this window arise from the combined effect of two nanoscale characteristic length scales: (i) if the ligament diameters are below the sizes of collision cascades (usually several nm), the ligament melts and breaks; (ii) once the ligament diameters are above the distance that defects migrate (depending on defects diffusivity) in the time interval between cascades (depending on the dose rate), the ligament behaves as a bulk material and tends to accumulate damage. In between these dimensions is the window of optimal length scales where the defect migration to the ligament surface is faster than the time between successive cascades, ensuring efficient defect recovery and radiation resistance. In-situ TEM observation of nanoporous (np) Ag (ligament size: 40 nm) [29] and np Au (ligament size: 30–50 nm) [30] upon heavy Kr ion irradiation demonstrated their significantly better radiation tolerance compared to the coarse-grained, fully dense counterparts.

Through a comprehensive study on the mechanical response of the model np Au, Hodge et al. demonstrated that, when the ligament size is below 500 nm, the foam strength follows a scaling law that is governed by ligament size in addition to relative density [31]. That is, the yield strength of a metallic foam can simply be increased by decreasing the ligament length scale [31,32]. For Au foams with ligaments of 15 nm in diameter, the ligament strength approaches the theoretical strength of Au [32].

W seems to be ideally suited as a base material for such an open-cell nanofoam, however, it has not yet been created due to its less noble properties. Therefore, it would be of great value and scientific interest to tailor such a novel material, which combines the beneficial properties of W with the positive attributes of nanofoams. Similar to np Au, np W is expected to have a ligament-size-dependent radiation resistance and mechanical behavior. In this work, nanoporous W made of nanocrystalline W grains and nanoscale W ligaments will be created for achieving the potential of extraordinary strength and concurrent radiation shielding capability.

A classical method to obtain np structures is selective dissolution of less noble elements from an alloy by chemical [33] and electrochemical [34,35] dealloying, which was mostly applied to noble model systems such as Au [33], Ag [35] and Cu [33,34,36]. In this work, we use a unique procedure involving severe plastic deformation (SPD) of immiscible binary metal systems [37,38] followed by selective phase dissolution of the unwanted phase. This avoids the steps of alloying and dealloying in the classical method and therefore lifts thermodynamic constraints. So far ultrafine porous Cu [39] and nanoporous Au [40,41] structures have been successfully manufactured by utilizing this strategy. In this procedure, the second phase is the key for successful nanostructuring via SPD and subsequent selective dissolution, which in general has to fulfill four requirements: (i) immiscible with W to avoid alloying and dealloying; (ii) ductile and soft to compensate for the brittle and hard W. Otherwise, SPD is challenging to proceed due to the mechanical limitations of the used dies (e.g. anvils used in high pressure torsion, HPT) [42]; (iii) chemically stable in air as SPD will be executed in air; (iv) more chemically active than W so that it can be selectively removed in a specific solution. Previous work indicates that the first three requirements can be easily fulfilled by Cu. And W-Cu composites with an average grain size of 10–20 nm have been successfully fabricated by HPT at room temperature [38,43,44]. The only concern is the last point, as W is less noble than Cu according to the standard electrode potential [45]. Therefore, to achieve reverse phase dissolution (i.e., selectively remove the noble Cu component and result in a porous structure of the relatively active W component) turns out to be the challenge. So far, it has been reported that the reverse phase dissolution can be achieved by controlling the etching conditions, e.g. by employing a metallic melt instead of an aqueous solution [46], or by using an etching system in which the more active component is passivated [47–49].

In general, the main objective of this work is to create novel np W foams and to investigate their mechanical behavior. We will firstly produce nanocrystalline (nc) W-Cu composites through a unique fabrication route of SPD and then obtain the np W foam structures by fulfilling selective dissolution of the nobler Cu component using an etching solution system in which the less noble W is chemically stable. Subsequently, we will characterize the microstructure of the created porous materials to analyze how the etching solutions affect the resulting np structures. In many radiation shielding applications, proper mechanical properties are a prerequisite [50,51]. Therefore, here we use depth-sensing nanoindentation to study the mechanical properties of the created W foam, as it enables determination of fundamental mechanical properties and parameters indicating the predominating deformation mechanism [31,40,41,52,53]. The yield strength and elastic modulus of the created nanoporous W will be determined and compared to the scaling law predictions of their macroscopic foam counterparts.

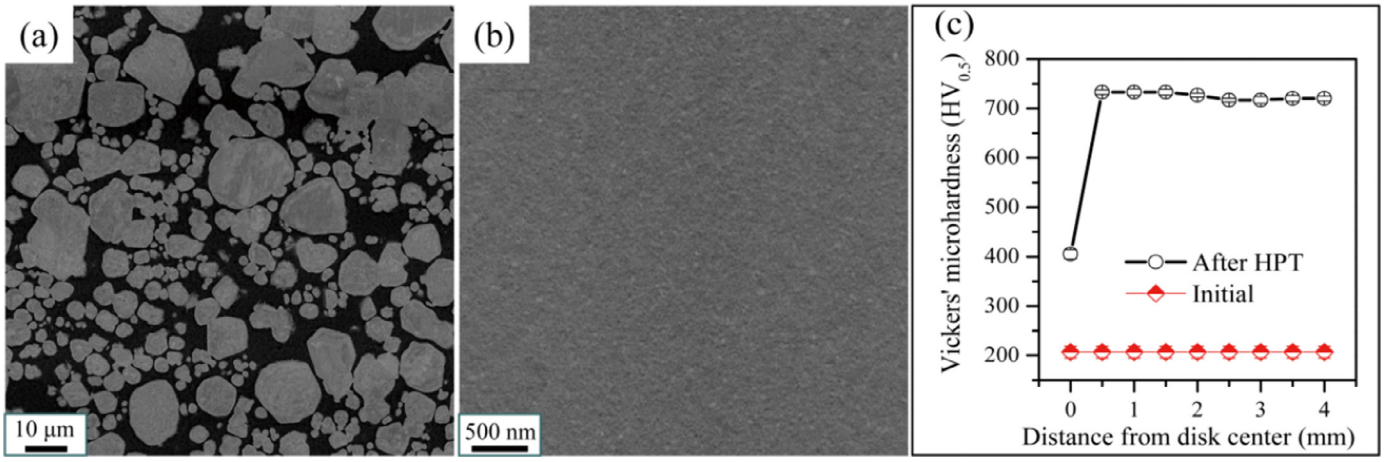

Fig. 1. Microstructure of the W-Cu composite before and after HPT: (a) SEM image of initial structure, (b) saturated microstructure after HPT (typically for radii ranging from ~1 to 4 mm), (c) microhardness before and after HPT.

2. Experimental procedures

2.1. Precursor synthesis

The approach to fabricate nc W-Cu composites is via the SPD method of HPT. A detailed introduction on HPT of immiscible W-Cu composite systems can be found in Refs. [38,43]. Due to the immiscibility of W and Cu at ambient temperatures, sharp W/Cu interfaces are expected, which is beneficial to achieve a fairly pure W skeleton structure after dealloying. Coarse-grained W-20 wt.% Cu composite materials (see Fig. 1a) purchased from Goodfellow (*England*) were used as starting material. This gives a Cu volume percentage ratio of 35% and an W:Cu atomic ratio of 58:42 ($W_{58}Cu_{42}$). HPT was performed on discs with a diameter of 8 mm and a thickness of 0.8~0.9 mm, and processed at a pressure of 7.5 GPa with a rotational speed of 1.2 rpm for above 60 turns to reach a saturated structure (typically at radii ranging from ~1 to 4 mm, as revealed by microstructure observation in Fig. 1b and Vickers' microhardness test in Fig. 1c). The resulting product is a disk with a diameter of 8 mm and a thickness of around 0.55 mm. Prior to reverse phase dissolution, an additional heat treatment was conducted at 300 °C for 1 h in a vacuum furnace to reduce the amount of forced mechanical mixing between W and Cu (about 5 at.% W dissolved in Cu and 4 at.% Cu in W for W-25 wt.% Cu was estimated in Ref. [38]). Note that 300 °C is around 30% of the melting point of Cu, even higher heat treatment temperatures will potentially lead to coarsening of the nc W-Cu composites, especially to preferential accumulation of Cu phase. Prior to heat treatment, the fabricated composite samples were subjected to grinding and mirror polishing on one side for microstructural observations. As shown in Fig. 1b, W and Cu components are uniformly distributed and the grain sizes are substantially decreased after HPT, resulting in a significant microhardness increase from ~200 to ~720 $HV_{0.5}$ (Fig. 1b). Note that for each data point shown in Fig. 1c, at least 3 indents were performed at a load of 500 g.

2.2. Foam processing

Porous W structures were developed by free corrosion of the nc W-Cu precursor. In Table 1, the used etching solution, the corresponding chemical etching mechanism and the etching time are given. Ammonium persulfate ($(NH_4)_2S_2O_8$) was selected as etchant, as its aqueous solution is often used to dissolve Cu products [54,55], and meanwhile the less noble W turns out to be chemically stable against their attack. The applied concentration of the used etchant enables a relative high etching speed. Etching was performed by just immersing 1/6 HPT disk (with one side polished) into the etching solution for a certain time. Here we should note that all surfaces of the specimen were etched, as they were all surrounded by the etching solution. After wards, the samples were taken from the beaker and transferred into distilled water for 30 min to remove the etchants. To remove tungsten oxides (WO_3) possibly formed because of hydrogen evolutional corrosion, samples were additionally immersed into 2 wt.% sodium hydroxide (NaOH) for 30 min, and eventually washed several times in distilled water and dried by warm air. Visual inspection showed that the samples lost their original metallic luster after etching, but no cracking or fragmentation was detected.

Table 1
Parameters used for porous W synthesis by reverse phase dissolution (i.e. selective dissolution of the nobler element) at room temperature.

Etchant	$(NH_4)_2S_2O_8$ (23 g/100 ml H_2O)
Etching mechanism	$Cu+(NH_4)_2S_2O_8 \rightarrow CuSO_4+(NH_4)_2SO_4$ $(NH_4)_2S_2O_8+2H_2O \rightarrow H_2SO_4+(NH_4)_2SO_4+H_2O_2$ $Cu+H_2O_2+H_2SO_4 \rightarrow CuSO_4+H_2O$
Etching time	1/6 HPT disk: 18 h; TEM sample: 18 h.

2.3. Microstructural characterization

The microstructure is characterized by a scanning electron microscope (SEM, *LEO 1525, Carl Zeiss GmbH, Germany*) equipped with an energy dispersive X-ray spectrometer (EDX). Prior to SEM observation, the surfaces were subjected to mechanical grinding by SiC paper and chemo-mechanical polishing by silicic acid solution. Here the polished surface of porous metals was obtained by polishing before etching. A femtosecond laser system [56] was used to produce cross-section specimens for sub-surface observation. The laser system contains a focused ion beam column (*Orsay Physics Ga^+ ion FIB*) and an integrated femtosecond laser (*OneFive Origami 10XP*). The femtosecond laser offers a fast processing of arbitrary structures, while the FIB allows a precise rework. Through EDX analysis, the overall composition of the investigated materials was determined.

A transmission electron microscope (TEM) JEOL 2100F (*JEOL, Tokyo, Japan*) operating at 200 kV was used for acquiring bright field (BF) and high-resolution (HR) TEM images. A TEM JEOL 2200F also operating at 200 kV was used for acquiring scanning

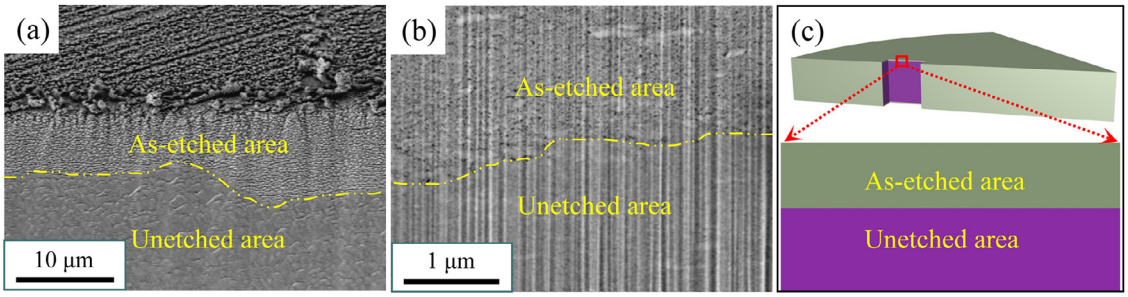

Fig. 2. Cross-sections of the nanocrystalline W-Cu precursor after etching in $(NH_4)_2S_2O_8$ for 18 h. (a): Femtosecond laser processed cross-section. (b): FIB reworked cross-section. The etching front is marked by a yellow dashed line. (c): Schematic drawing showing the location of the observed cross-section in the specimen. (For interpretation of the references to colour in this figure legend, the reader is referred to the web version of this article.)

TEM (STEM) images. TEM samples were prepared by mechanical polishing, dimpling with diamond paste as well as final Ar ion milling. The phase constitution and crystalline nature (single crystalline or polycrystalline) were determined by selected area electron diffraction (SAED). BF-TEM and HR-TEM analyses were utilized to document the microstructure on a nanometer scale. From HR-TEM images and the corresponding Fast Fourier Transform (FFT) patterns, lattice features (fringes) and spacings of the nanomaterial structure within the area of interest can be clearly seen, thus further discerning the crystalline nature and obtaining information on lattice defects. The combination of EDX mapping with STEM using a high-angle annular dark field (HAADF) mode was used to acquire the compositional information at the nanoscale especially at the interfaces (including GBs and phase boundaries (PBs)).

2.4. Mechanical testing

The mechanical properties, including the deformation behavior under compressive stress, yield strength and Young's modulus, were obtained by depth-sensing nanoindentation using a G200 Nanoindenter (*KLA Corporation, USA*) equipped with a Berkovich tip from Synton-MDP (Switzerland). Indentations were applied on the specimen surfaces polished before selective phase dissolution. For each specimen, 10 nanoindentation tests were conducted for ensuring the test accuracy and minimizing the experimental errors. All nanoindentation experiments were performed with a constant strain rate of 0.05 s^{-1}. The continuous stiffness measurement (CSM) method was applied to track hardness and modulus as a function of the indentation depth.

3. Experimental results

3.1. SEM microstructure observation

As the goal is to create a nanoporous bulk material, the depth-depended evolution of porosity is considered in Fig. 2a and b. Fig. 2c is a schematic drawing showing the location of the observed specimen cross-section. Note that the distances in the vertical direction of Fig. 2a and b are compressed by a factor of 0.71, as the cross-sections were horizontally titled by ~45° with respect to the viewing plane. The femtosecond laser processed cross-section is shown in Fig. 2a, where two layers with different morphology are clearly observed for each sample. EDX analysis indicates that Cu is absent in the as-etched region (upper layer, with a thickness of ~15 μm), confirming a complete removal of Cu via the $(NH_4)_2S_2O_8$ etching solution. This also indicates that the formed pores after the removal of Cu are interconnected, ensuring the deeper permeation of etching solution into the specimen and thus leading to an open-cell W foam structure in the as-etched region. The different appearances in as-etched and unetched regions (Fig. 2a) are probably due to the different ablation characteristics of nc W-Cu precursor and porous W during the laser ablation process. Besides, a homogeneous permeation of etching solution over the observed sample surface area is noticed, as the etching front appears rather parallel to the etched surface. The FIB reworked cross-section is given in Fig. 2b. It clearly unveils the porous structure nearby the etching front. In the as-etched region, pores are shown as dark contrast and uniformly distributed in the W matrix.

3.2. TEM characterization of various nanostructures

As noticed from Fig. 2, the formed pores and ligaments in $(NH_4)_2S_2O_8$ are much finer and challenging to resolve in the SEM images. Thus, to unveil the nanostructure of the nc W-Cu precursor (Fig. 1b) and np W produced using $(NH_4)_2S_2O_8$ solution (Fig. 2b), TEM techniques are employed. The observed surfaces in Fig. 3 are parallel to the HPT disk and located in the microstructure saturated region. Fig. 3a and e are STEM images using HAADF mode, which give a good mass contrast to distinguish different phases. As indicated by SAED patterns in Fig. 3d and h, the polycrystalline nature of the W grains remains unchanged. The absence of Cu phase in Fig. 3h demonstrates a complete removal of Cu in the as-etched nc W-Cu. This is in a good agreement with EDX analysis at the subsurface (Fig. 2). From the SAED pattern analysis, the bright phase in Fig. 3a and e are deduced to be W grains, which in unetched state (Fig. 3a) show no observable difference in both size and morphology from the as-etched condition (Fig. 3e). Thus, the morphology and size of W grains in nc W-Cu precursor are conserved into the resulting np W. Fig. 3b and c are low-mag and high-mag BF-TEM images of the nc W-Cu precursor, respectively. Many grains with an average size of ~15 nm are observed. Fig. 3f and g show the np W structures acquired by using $(NH_4)_2S_2O_8$ etching solution. It is characterized by interconnected pores with an average size of 20 nm and ligaments comprising of 1–3 W grains (~15–45 nm, on average 25 nm). As selective dissolution of Cu was processed without noticeably changing the grain structures, i.e., Cu nanoparticles are in-situ substituted by nanopores during the etching process, the pore size in the np W (Fig. 3e-g) is roughly regarded as the size of the Cu nanoparticles in the nc W-Cu precursor (Fig. 3a–c).

Fig. 4 shows an EDX mapping of the nc W-Cu precursor coupled with HAADF-STEM imaging, from which the distribution of detected elements (including W, Cu and O) are clearly revealed. Fig. 4c indicates that the grains with a bright contrast and the matrix with a dark contrast in Fig. 4a are W and Cu, respectively. The grains detected in Fig. 4b and c with an average size of ~15 nm are thus confirmed to be W grains. Three categories of W grains are herein observed: (i) W grains connected by type I GB, e.g., W grain 1 and 2 in Fig. 4a, (ii) W grains connected by type II GB, i.e., an intermediate layer consisting of W, Cu and O elements (Fig. 4a, marked by a yellow double headed arrow),

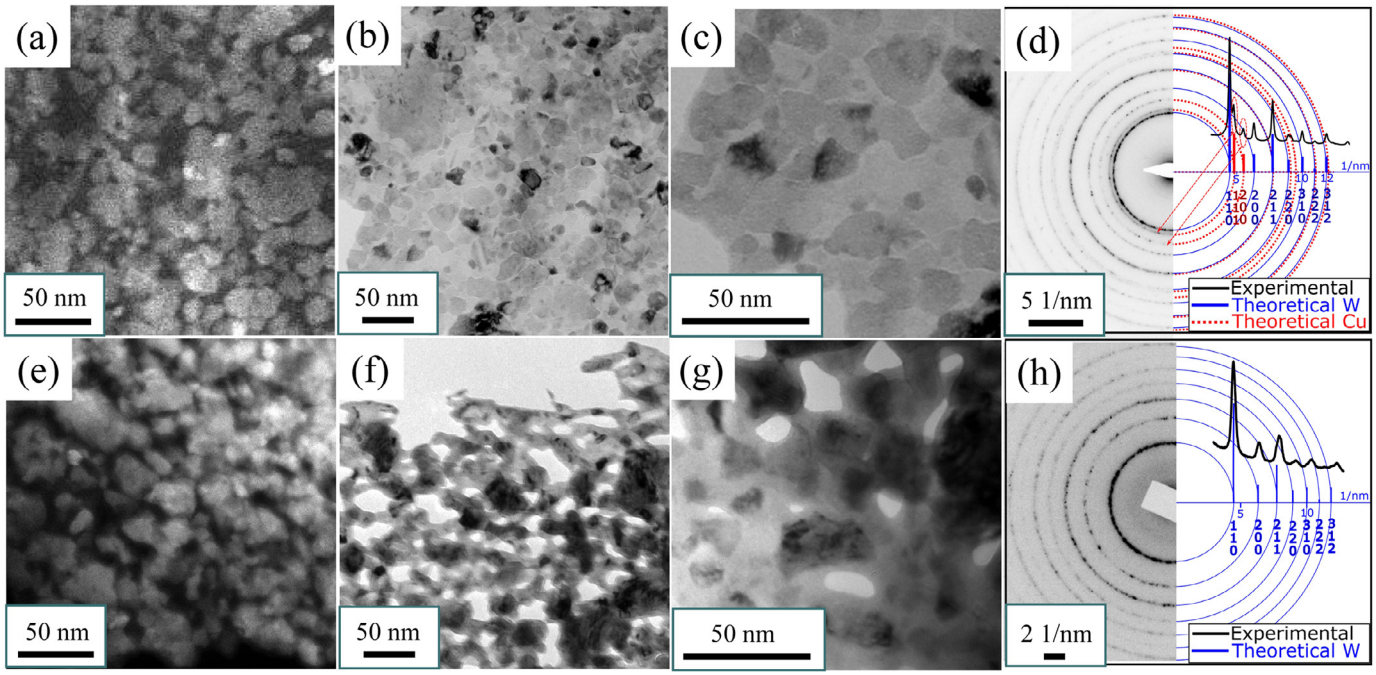

Fig. 3. Nanocrystalline W-Cu precursor (a–d) and nanoporous W (e–h). (a) and (e): STEM-HAADF images, (b) and (f): BF-TEM images, (c) and (g): higher magnified BF-TEM images, (d) and (h): SAED patterns. Note the dark contrast phases in (a) and (e) are Cu and pores, respectively.

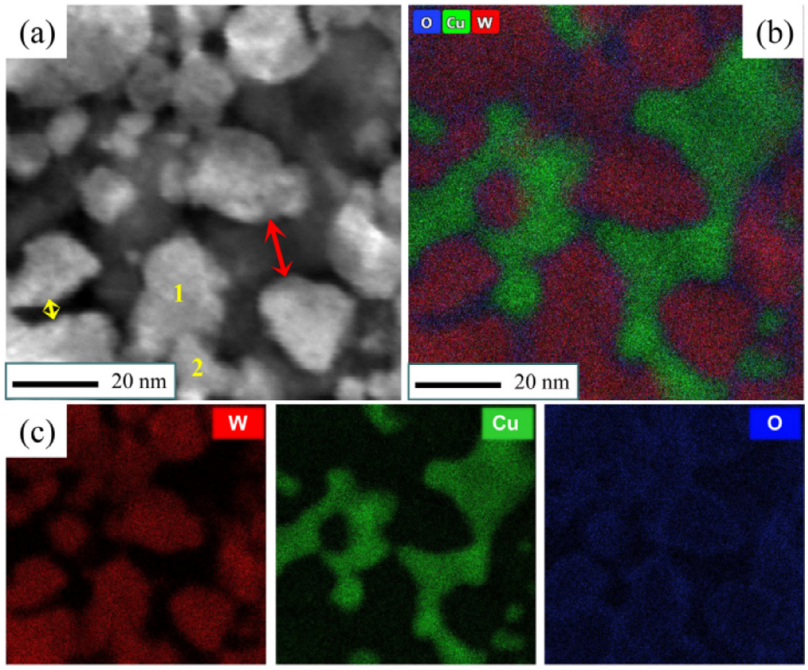

Fig. 4. Chemical composition distribution of W, Cu and O in the nanocrystalline W-Cu precursor: (a) HAADF-STEM image, (b) multiple element EDX mapping, (c) separated view of W, Cu and O. The double headed arrows with different colors represent different types of intermediate layers between two adjacent W grains. Two closely connected W grains are marked with number 1 and 2.

(iii) W grains separated by Cu nanoparticles (Fig. 4a, marked by a red double-headed arrow). In Fig. 4b W/Cu PBs are shown as a layer consisting W, Cu and O elements. Moreover, from the HAADF-STEM image (Fig. 4a) it is noticed that the brittle W grains are discontinuously distributed in the ductile Cu matrix. This is quite understandable because in the HPT process of hard-soft immiscible systems, the deformation is governed by strong plasticity in the softer Cu phase, together with heavy elongation and repeated fracture of the harder W particles [37,57]. HR-TEM images shown in Fig. 5 reveal the crystal lattice at the interfaces. Fig. 5a shows a clean and sharp W GB, which corresponds to type I GB in Fig. 4a. The type II GB and W/Cu PB in Fig. 4a are revealed as intermediate layers with a thickness of ~1–3 nm (Fig. 5b) and ~1–2 nm (Fig. 5c), respectively. Due to the coexistence of W, Cu and O elements (Fig. 3b and c), type II GBs (Fig. 5b) and W/Cu PBs (Fig. 5c) exhibit lattice structures completely different from the W and Cu grains. HR-TEM images in Fig. 6 show the crystal lattice of the tailored np W. W grains in the regions around the pore are connected by low-defective W GBs (i.e., type I W GB). No type II W GBs are observed in the tailored np W (Fig. 6a). As shown in

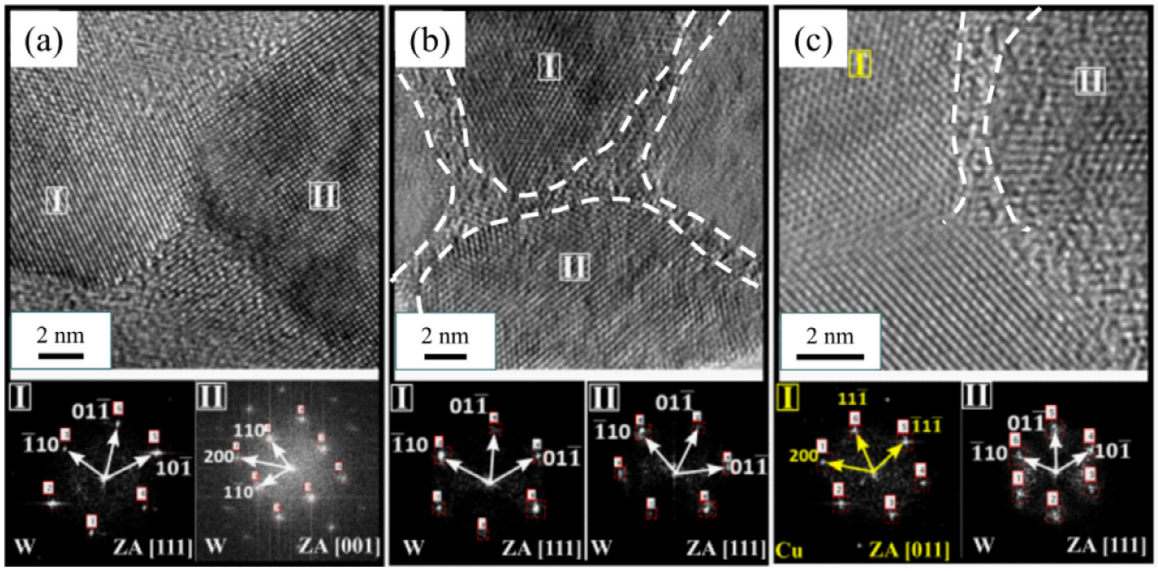

Fig. 5. HR-TEM images of nanocrystalline W-Cu precursor showing: (a) type I W GB, (b) type II W GB, (c) W/Cu PB. The FFT patterns for different grains are displayed below the corresponding HR-TEM image. White dashed lines are the indications for the regions of type II W GB and W/Cu PB.

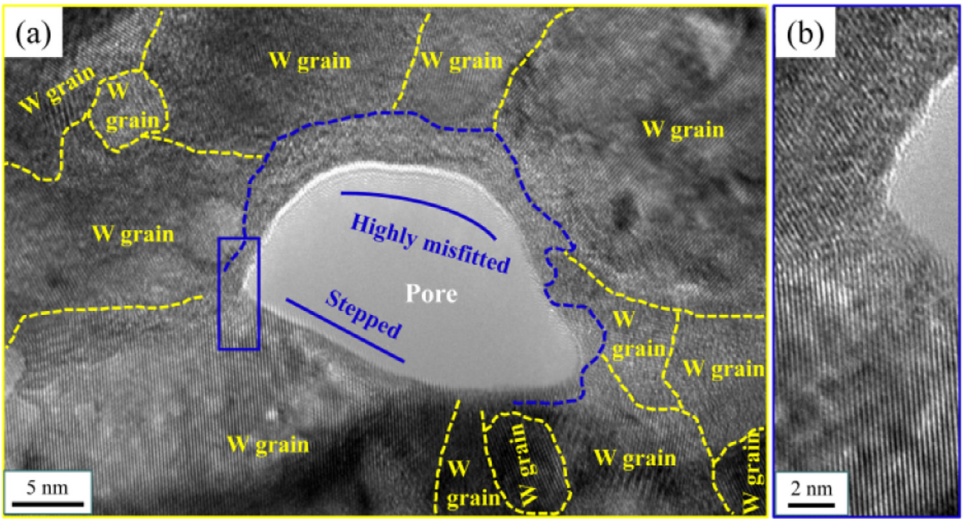

Fig. 6. (a) HR-TEM image of np W showing the lattice structures around a pore. W GBs are indicated by yellow dashed lines. A highly distorted area along the free surface (i.e. pore/W interface) is highlighted by a blue dashed line. (b) Higher magnified HR-TEM image showing the blue rectangular area given in (a). (For interpretation of the references to colour in this figure legend, the reader is referred to the web version of this article.)

detail in Fig. 6b, the W/pore interface (i.e., W free surface) appears to have many atomic kinks and lattice defects.

3.3. Nanoindentation test

Fig. 7a shows the load-displacement (*P-h*) indentation curves obtained from nanoindentation tests on the polished surface of the created W nanofoam. Solid nc W fabricated by HPT of coarse-grained, fully dense W at 300 °C with a saturated grain size of 130 nm is taken as a reference and compared to the created W nanofoam. As the goal of nanoindentation is to sense the mechanical response of an ensamble of ligaments and pores instead of the individual ligaments, an indentation depth deep enough to characterize the strength of the foams is a necessary prerequisite [58]. Therefore, based on the ligament size of the tested materials, a peak load of 670 mN was applied for the solid nc W, resulting in maximum indentation depths around 2000 nm. For the np W, the maximum indentation depth was controlled to 1000 nm, corresponding to an applied peak load of ~110 mN. Note that these two indent depths correspond to approximately 13% and 7% of the total thickness of the as-etched layers, respectively. The loading sections of the *P-h* curves for different indents on the sample surface are often overlapped, indicating a good reproducibility of the experiments. Fig. 7b and c show residual indent impressions on the polished surface. In comparison to the solid nc W (Fig. 7c), the residual indent impression of the created W nanofoam (Fig. 7b) reveals that the deformation is contained in the contact area with the involvement of minor cracking near the surface. Neither pileup of material nor deformation adjacent to the residual impression was observed.

The hardness and reduced Young's modulus values were calculated by analyzing the *P-h* indentation curves using the Oliver-Pharr method [59], and displayed in Fig. 8a and b versus displacement, respectively. The np W shows a nanoindentation behavior similar to the solid nc W. At indentation depths smaller than 250 nm, the np W and solid nc W appear to be harder than at larger indentation depths, which could be due to the indentation

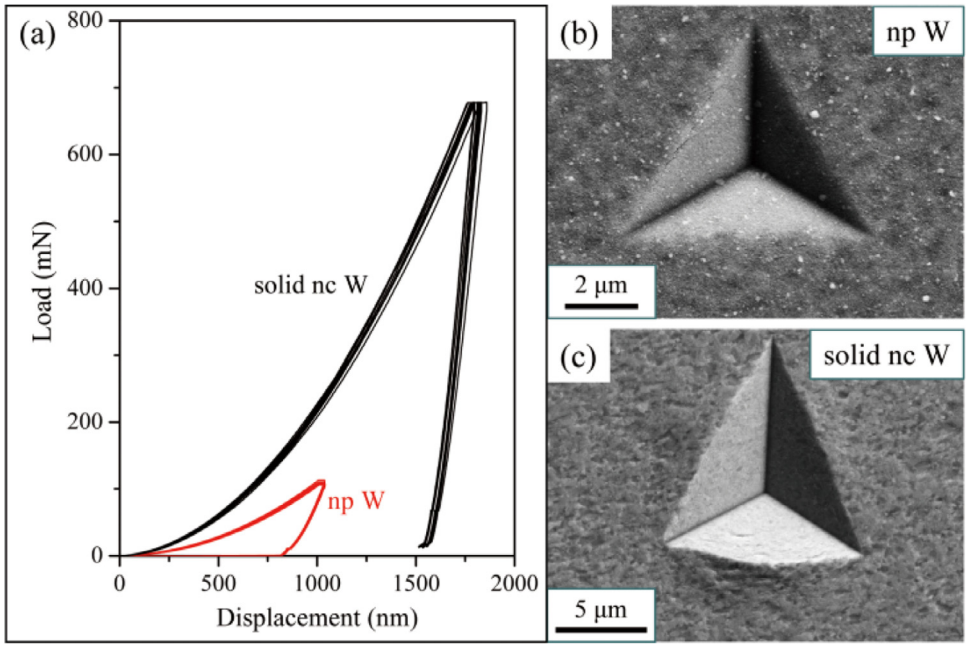

Fig. 7. Nanoindentation experiments on the polished surface of the created np W in comparison to solid nc W: (a) load versus displacement curves using a Berkovich tip, (b-c) SEM micrographs of the residual indent impressions.

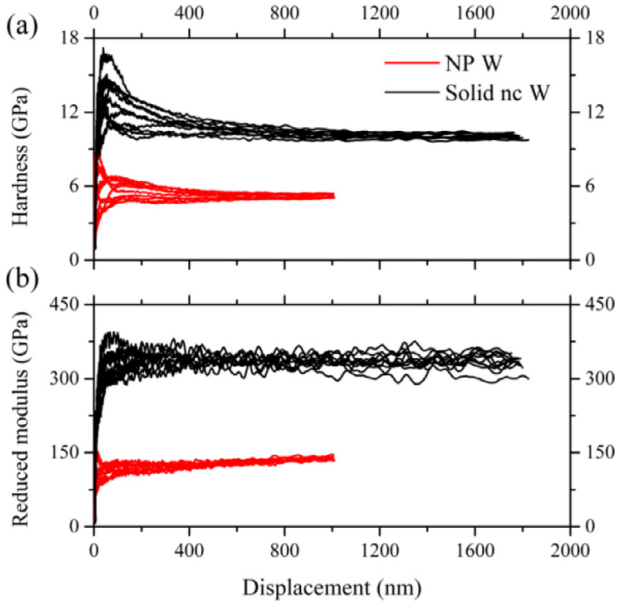

Fig. 8. Nanoindentation experiments on the polished surface of the created np W in comparison to the solid nc W: (a) hardness versus displacement, (b) reduced modulus versus displacement.

size effect [60] or contact imperfections. For indentation depths in excess of ~500 nm, an almost constant hardness of ~5.3(±0.3) GPa and ~10.3(±0.3) GPa is observed for the np W and the solid nc W, respectively. As observed in Fig. 8b, the reduced Young's modulus of the np W and solid nc W remains constant at 120.8 ± 5.8 GPa at indentation depths between 200 and 500 nm and at 335.8(±9.9) GPa at indentation depths ranging from 500 to 1500 nm, respectively.

Since the hardness H is proportional to the indentation flow stress σ via the constraint factor C^* by $H = C^* \cdot \sigma$ [61], the strength was assessed from the hardness values obtained by the indentation experiments described above. The value of C^* is related to the morphology of the plastic zone underneath the indenter tip and strongly depends on Poission's ratio ν [21,62]. In the case of dense materials ($\nu = 0.28$ for solid W [63]), the yield strength σ_s is related to the hardness H by $\sigma_s = 1/3\ H$ ($C^* = 3$). Thus, the yield strength assessed from the hardness data is 3.4 GPa for the solid nc W. However, in the case of porous metals, the determination of C^* demands some more considerations. The Poisson's ratio υ_f for the tailored np W foam with a porosity of 0.35 could be predicted by following the analytical model developed by Pal for a concentrated pore-solid composite [63,64]:

$$\upsilon_f(\varphi) = (1 + \upsilon_0)\left(1 - \frac{\varphi}{\varphi_{\max}}\right)^{\varphi_{\max}/4} - 1 \quad (1)$$

where, φ is the porosity level, $\varphi_{\max}$ is the maximum packing volume fraction of pores with spherical or near spherical morphology, ν_0 is the Poisson's ratio of the solid, i.e., 0.28 [63]. For the tailored np W, the maximum packing volume fraction of pores $\varphi_{\max}$ is taken as 0.637 for random close packing of monosized spherical pores in the analytical model [63]. Thus, the Poisson's ratio υ_f is analytically predicted as 0.127 by Eq. (1), which lays between that of fully dense W ($\nu = 0.28$ [63]) and of a low-porosity W cellular solid ($\nu = 0$ [21]). This non-zero Poisson's ratio for np foams is also reported by Balk et al. [65], whose tensile and compression tests indicated a Poission ratio about 0.16 for np Au. According to Ref. [62], in which the constraint factor C^* is described to increase rapidly from unity toward the standard quoted value of 3 as the Possion's ratio increases from zero, $\nu = 0.127$ results in a constraint factor C^* of ~2.6. Accordingly, a yield strength of 2.04 GPa is determined. The yield strength of macroscopic W foam counterparts (i.e. open-cell W materials with porosity at length scales larger than that of nanoporous foams) can be predicted by the Gibson and Ashby scaling law:

$$\sigma^* = C_1 \sigma_s \left(\frac{\rho^*}{\rho_s}\right)^n \quad (2)$$

where σ_s and ρ_s are the yield strength and the density of the fully dense material, and ρ^* is the density of porous W [21]. ρ^*/ρ_s is the relative density of porous W, and C_1 and n are constants. The proportionality C_1 describes the cell geometry and density exponent

n depends on the formation mechanism of the cell. Experimental data indicates that a wide range of open-cell foam materials can be adequately described by $C_1 = 0.3$ and $n = 1.5$ [21]. Using the yield strength of the solid pure W with an average grain size of ~130 nm ($\sigma_s = 3.4$ GPa), the scaling law predicts that the yield strength of macroscopic foam W with a relative density of 0.65 is 0.53 GPa. In comparison, the tailored np W exhibits a yield strength ~3.8 times higher than the scaling law predicted macroscopic W foam. This discrepancy is likely to be influenced by mechanical size effects (i.e. differences in grain/ligament sizes), which will be discussed in Section 4.2.

The Young's modulus of the np W and the solid nc W is extracted from the unloading curves based on the standard expression of nanoindentation theory [59], which takes both the elastic response of the indenter and indented material into account:

$$\frac{1}{E_r(\varphi)} = \frac{1-\upsilon_d^2}{E_d} + \frac{1-\upsilon_f^2(\varphi)}{E_f(\varphi)} \tag{3}$$

The elastic modulus E_d and Poisson's ratio ν_d of diamond were used for the indenter properties, i.e., $E_d = 1140$ GPa and $\nu_d = 0.07$ [40]. The reduced Young's modulus of the tailored np W and solid nc W is measured as 120.8 and 335.8 GPa, respectively, resulting in a Young's modulus of 133.0 and 437.3 GPa as described by Eq. (3). In analogy to Eq. (2), the Young's modulus of the macroscopic W foam counterparts can also be predicted by the Gibson and Ashby scaling law:

$$E^* = C_2 E_s \left(\frac{\rho^*}{\rho_s}\right)^n \tag{4}$$

where E_s is the Young's modulus of the solid W, the proportionality constant C_2 describes the cell geometry and the density exponent n describes the elastic cell formation via ligament bending [21]. Experimental data obtained from open-cell foam materials are usually well fitted by using $C_2 = 1$ and $n = 2$. Using the Young's modulus of the solid pure W with an average grain size of 130 nm as a reference, the scaling law predicts a Young's modulus of 184 GPa for the macroscopic W foam, which is in the same order of magnitude as the determined one for the np W (133 GPa).

4. Discussion

As introduced before, the $(NH_4)_2S_2O_8$ solutions can be utilized for the successful removal of the nobler Cu phase in the fabricated nc W-Cu precursor. It is well known that the formation of a np structure is a thermally activated process and that the nanoporosity evolution is controlled by surface diffusion of the remaining element along the metal/solution interfaces [65–67]. Therefore, in this section the formation mechanism for the porous structure is elucidated based on the Arrhenius equation for surface diffusion [68]. Moreover, nanoindentation tests revealed that the np W created by using $(NH_4)_2S_2O_8$ solution exhibits an outstanding yield strength outperforming scaling law predictions of the macroscopic W foams. Thus, at the end of this section, the ultra-high strength in the created np W foams are interpreted.

4.1. Porous structure formation mechanism

Fig. 3 shows that the grain size and structure of the nc W-Cu precursor are retained into the created np W by using $(NH_4)_2S_2O_8$ etching solution. This indicates that the $(NH_4)_2S_2O_8$ solution has little influence on the surface diffusion of W atoms. Thus, the volume percentage, size and distribution of the second Cu phase in the nc W-Cu precursors are very important for the final np W structures when using $(NH_4)_2S_2O_8$ as the etchant.

The high-resolution microstructure observations for the nc W-Cu precursor and the created np W (Figs. 3–6) indicates a local surface diffusion of W atoms over a short distance during the etching process. Such a surface diffusion is deduced to take place at type II W GBs (Fig. 5b) and W/Cu PBs (Fig. 5c) at the nanoscale. As illustrated in Fig. 9, adatoms, step adatoms and kink atoms described in the terrace ledge kink model [69] (displayed as dark grey spheres) are formed along these interfaces after Cu atoms (shown as orange spheres) are etched away. As compared to the surface and bulk W atoms (shown as bright grey spheres), these atoms are much more mobile, as fewer bonds need to be broken to form an adatom-vacancy pair, leading to a decrease in the activation energy for surface diffusion [69]. Driven by the reduction of surface free energy [70], the rearrangement of these mobile W atoms occurs to form low-defective W GBs instead of defect-rich W GBs (Fig. 6).

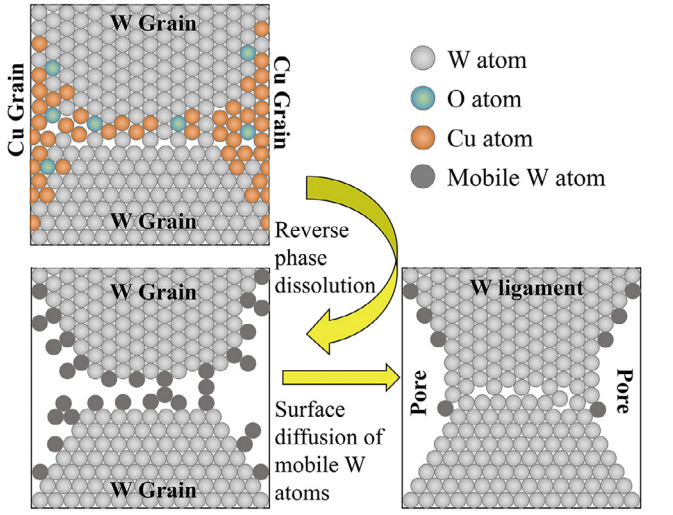

Fig. 9. Schematic illustration for the formation of nanoporous W structure by selective phase dissolution of the nanocrystalline W-Cu precursor in $(NH_4)_2S_2O_8$ etching solution. Cu grains are located respectively at the left and right sides of W grains. A diffusion of W atoms over a short range takes place for the formation of strong low-defective W GBs.

Figs. 4 and 5 reveal the existence of Cu at type II W GBs and W/Cu PBs in the nc W-Cu precursor. This can be explained by the forced mutual solid solution of W and Cu during HPT and subsequent insufficient annealing (300 °C for 1 h). Moreover, a low concentration of O, preferably at type II W GBs and W/Cu PBs, is unexpectedly detected. The low amount of O detected in the regions of W and Cu grains is quite understandable, as the surface may get oxidized during and after TEM specimen preparation. A more careful observation of Fig. 4c shows that O is much more detectable in W than in Cu. This phenomenon is quite abnormal, as in comparison to W, Cu is more active in the reaction with O and tends to have a higher solubility with O. As seen in Fig. 4a, which displays a good depth contrast, W is much thicker than Cu because W is more sputtering-resistant to the bombardment of Ar ions during the TEM sample preparation by Ar ion beam thinning. A thicker W layer gives more O signal than the thinner one. Therefore, such an abnormal phenomenon is presumably caused by the thickness difference in the two different phases, which apparently overwhelms the difference in the chemical activity and solubility. The O originally existing in the coarse-grained W-Cu (trace amount, not being able to be detected by EDX analysis, introduced during its production history) probably contributes to the comparatively high O concentration at type II W GBs and W/Cu PBs (Fig. 4), as O tends to segregate preferentially at interfaces instead of inside grains during the fabrication [71–73].

According to the phase diagram of W-O [74] and Cu-O [75], the existing phases at low oxygen levels should be W, Cu, WO_3 and Cu_2O. Assuming that the oxygen-containing intermediate layers (including type II W GBs and W/Cu PBs) consist of an ~1 nm

WO_3 layer around W grains (15 nm on average) and ~1 nm Cu_2O layer on Cu grains (20 nm on average), a simple calculation based on mixture rules gives an oxygen amount of 0.58 wt.% (4.8 at.%). This value is actually much higher than the real value, as the lattice structure in Fig. 5 shows that Cu and W at type II W GBs and W/Cu PBs are not fully oxidized. However this overestimated O value confirms that oxygen is at a low level state and would exist as WO_3 and Cu_2O. Impurities such as O would decrease the strength of W GBs and thus embrittle W based materials [76]. However, as demonstrated by the high-resolution interface analysis (Figs. 5 and 6), the detrimental O can be removed presumably in the form of Cu_2O during the etching process and possibly as WO_3 during the immersing in NaOH solution.

4.2. Interpretation of the ultra-high strength

The residual nanoindentation impressions in Fig. 7 reveal that the deformation of the created np foam is confined to the area under the indenter with the involvement of minor cracking near the surface. This indicates that the residual impression of the np W is predominantly the result of plastic flow and the ligaments in the np W are plastically deformable [58]. In analogy to np Au foams [32,77,79], the deviation in the yield strength from the scaling law predicted macroscopic foam counterparts is also noticed for the tailored np W foams. The Gibson and Ashby scaling law is predominantly valid for homogeneous macroscopic foam structures with ligaments $L >> 500$ nm and relative density $\rho^*/\rho_s < 0.1$ [31]. For the tailored W foam with a ligament size of 25 nm and a relative density of 0.65, as interpreted below in detail, the observed differences between the experimental data and the Ashby and Gibson model predictions are due to its nanoscale microstructure and its high relative density.

Many researchers have observed that the effect of ligament size on ligament strength is evident when the ligament size is at the nanoscale [31,78,79]. There are also several explanations for such a size effect [31,80,81]. Based on the research of the plastic behavior of np Au foams, Hodge et al. revealed that the yield strength of the individual ligaments (σ_{lig}) is dependent on the ligament size (L) by following the Hall-Petch-like equation given below [31]:

$$\sigma_{lig} = \sigma + kL^{-1/2} \tag{5}$$

where k is a material constant. By incorporating Eq. (5) into Ashby and Gibson's model expression, a new scaling law given as Eq. (6) is formed [31]:

$$\sigma^* = 0.3\left(\frac{\rho^*}{\rho_s}\right)^{3/2}(\sigma + kL^{-1/2}) \tag{6}$$

However, this new scaling law is accurately applied to np foams with a relative density lower than 0.3 [31]. At even higher relative densities, Eq. (7) including the corrections to the equation of the density is developed to better rationalize the observed differences between the experimental data and Ashby and Gibson's model predictions [82]:

$$\sigma^* = 0.23\left(\frac{\rho^*}{\rho_s}\right)^{3/2}\left[1 + \left(\frac{\rho^*}{\rho_s}\right)^{1/2}\right](\sigma + kL^{-1/2}) \tag{7}$$

For the tailored np W with a relative density of 0.65 and an average ligament size of 25 nm, the Hall-Petch constants for tungsten ($H_0 = 350\ \mathrm{kg/mm^2}$, $k_y = 10\ \mathrm{kg/mm^{-3/2}}$, given in terms of hardness) [83] were used for the yield stress calculation of the individual ligaments by applying Eq. (5). As a result, a yield strength of 1.21 and 1.67 GPa is predicted by Eqs. (6) and (7) for the tailored np W, respectively. In comparison to 0.53 GPa predicted by Gibson and Ashby scaling law for the macroscopic foam counterparts, it is noticed that the nanoscale ligament size contributes dominantly to the ultra-high yield strength of the tailored np W foam. Eq. (7) provides a better fit to the experimentally determined strength value (2.04 GPa), revealing the high relative density plays also a role to the ultra-high strength. Moreover, it should be mentioned that the ligaments produced by the used unique foam processing method have a distinct nanocrystalline structure. Thus, the nanostructured grains in the np W would act as an additional strengthening effect, since the high density of GBs would effectively inhibit the transmission of dislocations from adjacent grains, resulting in dislocation pile-up and thus even higher yield stresses.

5. Conclusions

Aiming to satisfy the need for advanced high performance materials that can endure harsh irradiation environments, nanoporous W with ultra-strong ligaments is created by applying a unique technique. This consists of the fabrication of nanocrystalline W-Cu precursors by severe plastic deformation and reverse selective dissolution of the nobler Cu phase. The research results show that in the used $(NH_4)_2S_2O_8$ etching solutions Cu can be efficiently removed while the less noble W stays unattacked. Moreover, the W grain structure of the nanocrystalline W-Cu precursor is well retained during the etching process, indicating that the $(NH_4)_2S_2O_8$ solution has little influence on the surface diffusion of W atoms. Nevertheless, owing to the creation of mobile W atoms at the interfaces after the removal of Cu atoms, surface diffusion over a short range occurs to form low-defective W grain boundaries. As a result, strong-bonded and interconnected W ligaments consisting of 1–3 W nanocrystals are formed in the tailored porous structure. Nanoindentation tests reveal that the yield strength of the nanoporous W reaches up to 2.04 GPa, which is ~3.8 times higher than the Gibson and Ashby scaling law predictions of the macroscopic foam counterparts. By adopting new scaling equations to rationalize the deviation between the experimental data and the Gibson and Ashby scaling law predictions, it is revealed that the ultra-high strength of the tailored nanoporous W is derived from its nanoscale ligament size, its high relative density and its distinct nanocrystalline architecture.

It is worth to mention that, by adopting the new scaling laws proposed by Hodge [31] and Fan [82] et al., this work provides an explanation for the discrepancy in the yield strength between the experimental values and the Gibson-Ashby scaling law prediction values. However, as the relative density and the internal structures (e.g. ligament size) of the created nanoporous W are not varied, the rationality of the adopted new scaling laws in predicting the yield strength of nanoporous W with different relative densities and internal structures remains an open question. Therefore, in our future work, nanoporous W with tunable relative densities will be developed by using different nc $W_{1-x}Cu_x$ (X, the weight percentage of Cu) precursors, which are produced by severe plastic deformation of $W_{1-x}Cu_x$ powers or bulk composites. Besides, to investigate the link of internal porous structure to the mechanical properties, porous W with coarsened ligament sizes may be developed by vacuum thermal dealloying [84] of a nc $W_{1-x}Cu_x$ percursor at varying temperatures. As the grain textures changes with the degree of the severe plastic deformation [37,38], reverse phase dissolution of a coarse-grained $W_{1-x}Cu_x$ with different severe plastic deformation may be an another option to create porous W for addressing the internal structure influence on the mechanical properties of metallic foams.

This work for the first time evolves the fabrication of low density and ultra-strong nanoporous W on a bulk scale. Moreover, it is worth pointing out that the developed reverse phase dissolution method is generally applicable. Thus, it will facilitate developments of other attractive nanoporous active metals which are difficult to obtain using a classical electrochemical dealloying approach. The promising mechanical results of nanoporous tungsten will serve as

a foundation for forthcoming related scientific studies and engineering applications. The created nanoporous tungsten itself serves an model for promoting our basic understanding of foam response in an extreme radiation environment.

Author contributions

M.Z. designed the experiment, fabricated and characterized the materials, analyzed the porous structure formation mechanism and interpreted the ultra-high strength of the created nanoporous materials. I.I. conducted the TEM imaging presented in Figs. 3a, 3e, 5 and 6. M.J.P. performed the cross-section cutting and afterwards SEM imaging. M.W. conducted the nanoindentation tests. This work was carried out with the guidance and supervision of D.K. M.Z. wrote the paper with contributions from all authors.

Declaration of Competing Interest

None

Acknowledgment

This work is funded by the Austrian Science Fund (FWF) under Lise Meitner project No. M 2405-N36 (IRRESIST). D.K., I.I. and M.W. kindly acknowledge the financial support by the European Research Council (ERC) under the grant No. 771146 (TOUGHIT). The Austrian Research Promotion Agency (FFG) in the project 3DnanoAnalytics (FFG-No. 858040) is also acknowledged. The authors would like to thank Reinhard Pippan and Lisa Krämer for their valuable suggestions on high pressure torsion of the samples, thank Christoph Gammer for the STEM/EDX mapping presented in Fig. 4, thank Zhuo Chen for the TEM imaging in Fig. 3b and c. The suggestions of Jinming Guo, Julian Rosalie and Zaoli Zhang in the TEM sample fabrication and imaging are highly appreciated.

References

[1] M. Rieth, S.L. Dudarev, S.M. Gonzalez De Vicente, J. Aktaa, T. Ahlgren, S. Antusch, D.E.J. Armstrong, M. Balden, N. Baluc, M.F. Barthe, W.W. Basuki, M. Battabyal, C.S. Becquart, D. Blagoeva, H. Boldyryeva, J. Brinkmann, M. Celino, L. Ciupinski, J.B. Correia, A. De Backer, C. Domain, E. Gaganidze, C. García–Rosales, J. Gibson, M.R. Gilbert, S. Giusepponi, B. Gludovatz, H. Greuner, K. Heinola, T. Höschen, A. Hoffmann, N. Holstein, F. Koch, W. Krauss, H. Li, S. Lindig, J. Linke, C. Linsmeier, P. López–Ruiz, H. Maier, J. Matejicek, T.P. Mishra, M. Muhammed, A. Muñoz, M. Muzyk, K. Nordlund, D. Nguyen–Manh, J. Opschoor, N. Ordás, T. Palacios, G. Pintsuk, R. Pippan, J. Reiser, J. Riesch, S.G. Roberts, L. Romaner, M. Rosiński, M. Sanchez, W. Schulmeyer, H. Traxler, A. Ureña, J.G. van der Laan, L. Veleva, S. Wahlberg, M. Walter, T. Weber, T. Weitkamp, S. Wurster, M.A. Yar, J.H. You, A. Zivelonghi, Recent progress in research on w materials for nuclear fusion applications in Europe, J. Nucl. Mater. 432 (2013) 482–500.
[2] J.P. McCaffrey, H. Shen, B. Downton, E. Mainegra–Hing, Radiation attenuation by lead and non–lead materials used in radiation shielding garments, Med. Phys. 34 (2007) 530–537.
[3] Y. Iwamoto, R.M. Ronningen, Attenuation of ambient dose equivalent from neutrons by thick concrete, cast iron and composite shields for high energy proton, ^{3}He, ^{48}Ca and ^{238}U ions on Cu targets for shielding design, Nucl. Instrum. Methods B 269 (2011) 353–363.
[4] S. Agosteo, A. Mereghetti, E. Sagia, M. Silari, Shielding data for hadron–therapy ion accelerators: attenuation of secondary radiation in concrete, Nucl. Instrum. Methods B 319 (2014) 154–167.
[5] S. Kobayashi, N. Hosoda, R. Takashima, W alloys as radiation protection materials, Nucl. Instrum. Methods A 390 (1997) 426–430.
[6] S. Chen, M. Bourham, A. Rabiei, Neutrons attenuation on composite metal foams and hybrid open–cell Al foam, Radiat. Phys. Chem. 109 (2015) 27–39.
[7] J. Pamela, A. Bécoulet, D. Borba, J.L. Boutard, L. Horton, D. Maisonnier, Efficiency and availability driven R&D issues for demo, Fusion Eng. Des. 84 (2009) 194–204.
[8] S.J. Zinkle, L.L. Snead, Designing radiation resistance in materials for fusion energy, Annu. Rev. Mater. Res. 44 (2014) 241–267.
[9] J. Knaster, A. Moeslang, T. Muroga, Materials research for fusion, Nat. Phys. 12 (2016) 424–434.
[10] O. El-Atwani, J.A. Hinks, G. Greaves, S. Gonderman, T. Qiu, M. Efe, J.P. Allain, In-situ tem observation of the response of ultrafine- and nanocrystalline-grained tungsten to extreme irradiation environments, Sci. Rep. 4 (2014) 4716.
[11] O. El-Atwani, A. Suslova, T.J. Novakowski, K. Hattar, M. Efe, S.S. Harilal, A. Hassanein, In-situ TEM/heavy ion irradiation on ultrafine-and nanocrystalline–grained tungsten: effect of 3MeV Si, Cu and W ions, Mater. Charact. 99 (2015) 68–76.
[12] S.J. Zinkle, G.S. Was, Materials challenges in nuclear energy, Acta Mater. 61 (2013) 735–758.
[13] V. Philipps, Tungsten as material for plasma-facing components in fusion devices, J. Nucl. Mater. 415 (2011) S2–S9.
[14] S. Kajita, W. Sakaguchi, N. Ohno, N. Yoshida, T. Saeki, Formation process of tungsten nanostructure by the exposure to helium plasma under fusion relevant plasma conditions, Nucl. Fusion 49 (2009) 95005.
[15] O. El-Atwani, M. Efe, B. Heim, J.P. Allain, Surface damage in ultrafine and multimodal grained tungsten materials induced by low energy helium irradiation, J. Nucl. Mater. 434 (2013) 170–177.
[16] M.J. Baldwin, R.P. Doerner, Formation of helium induced nanostructure 'fuzz' on various tungsten grades, J. Nucl. Mater. 404 (2010) 165–173.
[17] H. Kurishita, H. Arakawa, S. Matsuo, T. Sakamoto, S. Kobayashi, et al., Development of nanostructured tungsten based materials resistant to recrystallization and/or radiation induced embrittlement, Mater. Trans. 54 (2013) 456–465.
[18] T.S. Byun, K. Farrell, Irradiation hardening behavior of polycrystalline metals after low temperature irradiation, J. Nucl. Mater. 326 (2004) 86–96.
[19] N.B. Heubeck, Nuclear fuel elements made from nanophase materials, U.S. Patent 5,805,657, 1998.
[20] M.F. Ashby, A.G. Evans, N.A. Fleck, L.J. Gibson, J.W. Hutchinson, H.N.G. Wadley, Metal foams: a Design Guide, 1st Ed, Butterworth–Heinemann, Burlington, 2000.
[21] L.J. Gibson, M.F. Ashby, Cellular solids, Structure and Properties, 2nd ed, Cambridge University Press, Cambridge (UK), 1997.
[22] S. Xu, M. Bourham, A. Rabiei, A novel ultra–light structure for radiation shielding, Mater. Design 31 (2010) 2140–2146.
[23] V.S. Deshpande, M.F. Ashby, N.A. Fleck, Foam topology: bending versus stretching dominated architectures, Acta Mater 49 (2001) 1035–1040.
[24] C. Linsmeier, M. Rieth, J. Aktaa, T. Chikada, A. Hoffmann, J. Hoffmann, A. Houben, H. Kurishita, X. Jin, M. Li, A. Litnovsky, S. Matsuo, A. von Müller, V. Nikolic, T. Palacios, R. Pippan, D. Qu, J. Reiser, J. Riesch, T. Shikama, R. Stieglitz, T. Weber, S. Wurster, J.H. You, Z. Zhou, Development of advanced high heat flux and plasma–facing materials, Nucl. Fusion 57 (2017) 092007.
[25] S. Wurster, N. Baluc, M. Battabyal, T. Crosby, J. Du, C. García–Rosales, A. Hasegawa, A. Hoffmann, A. Kimura, H. Kurishita, R.J. Kurtz, H. Li, S. Noh, J. Reiser, J. Riesch, M. Rieth, W. Setyawan, M. Walter, J.H. You, R. Pippan, Recent progress in R&D on w alloys for divertor structural and plasma facing materials, J. Nucl. Mater. 442 (2013) 181–189.
[26] Y. Matsukawa, S.J. Zinkle, One–dimensional fast migration of vacancy clusters in metals, Science 318 (2007) 959–962.
[27] P.A. Thorsen, J.B. Bilde–Sorensen, B.N. Singh, Bubble formation at grain boundaries in helium implanted copper, Scr. Mater. 51 (2004) 557.
[28] E.M. Bringa, J.D. Monk, A. Caro, A. Misra, L. Zepeda-Ruiz, et al., Are nanoporous materials radiation resistant? NANO LETT 12 (2012) 3351–3355.
[29] C. Sun, D. Bufford, Y. Chen, M.A. Kirk, Y.Q. Wang, M. Li, H. Wang, S.A. Maloy, X. Zhang, In situ study of defect migration kinetics in nanoporous ag with enhanced radiation tolerance, Sci. Rep. 4 (2014) 3737.
[30] J. Li, C. Fan, J. Ding, S. Xue, Y. Chen, Q. Li, H. Wang, X. Zhang, In situ heavy ion irradiation studies of nanopore shrinkage and enhanced radiation tolerance of nanoporous au, Sci. Rep. 7 (2017) 39484.
[31] A.M. Hodge, J. Biener, J.R. Hayes, P.M. Bythrow, C.A. Volkert, A.V. Hamza, Scaling equation for yield strength of nanoporous open–cell foams, Acta Mater 55 (2007) 1343–1349.
[32] C.A. Volkert, E.T. Lilleodden, D. Kramer, J. Weissmüller, Approaching the theoretical strength in nanoporous Au, Appl. Phys. Lett. 89 (2006) 061920.
[33] Z. Zhang, Y. Wang, Z. Qi, W. Zhang, J. Qin, J. Frenzel, Generalized fabrication of nanoporous metals (Au, Pd, Pt, Ag, and Cu) through chemical dealloying, J. Phys. Chem. C 113 (2009) 12629–12636.
[34] X. Luo, R. Li, L. Huang, T. Zhang, Nucleation and growth of nanoporous copper ligaments during electrochemical dealloying of Mg–based metallic glasses, Corros. Sci. 67 (2013) 100–108.
[35] C. Zhang, J. Sun, J. Xu, X. Wang, H. Ji, C. Zhao, Z. Zhang, Formation and microstructure of nanoporous silver by dealloying rapidly solidified Zn–Ag alloys, Electrochim. Acta 63 (2012) 302–311.
[36] B. Lin, M. Döbeli, S. Mudie, A. Hawley, P. Hodgson, L. Kong, R. Spolenak, L.F. Dumée, An in–situ small angle x ray scattering analysis of nanopore formation during thermally induced chemical dealloying of brass thin foils, Sci. Rep. 8 (2018) 15419.
[37] A. Bachmaier, J. Schmauch, H. Aboulfadl, A. Verch, C. Motz, On the process of co–deformation and phase dissolution in a hard–soft immiscible cuco alloy system during high–pressure torsion deformation, Acta Mater 115 (2016) 333–346.
[38] K.S. Kormout, R. Pippan, A. Bachmaier, Deformation–induced supersaturation in immiscible material systems during high–pressure torsion, Adv. Eng. Mater. 19 (2017) 1600675.
[39] M. Kreuzeder, M. Abad, M. Primorac, P. Hosemann, V. Maier, D. Kiener, Fabrication and thermo–mechanical behavior of ultra–fine porous copper, J. Mater. Sci. 50 (2015) 634–643.
[40] A. Leitner, V. Maier–Kiener, D. Kiener, High temperature flow behavior of ultra–strong nanoporous Au assessed by spherical nanoindentation, Nanomaterials 8 (2018) 366.

[41] A. Leitner, V. Maier–Kiener, J. Jeong, M.D. Abad, P. Hosemann, S.H. Oh, D. Kiener, Interface dominated mechanical properties of ultra–fine grained and nanoporous au at elevated temperatures, Acta Mater 121 (2016) 104–116.
[42] R. Pippan, S. Scheriau, A. Hohenwarter, M. Hafok, Advantages and limitations of HPT: a review, Materials Science Forum 584–586 (2008) 16–21.
[43] I. Sabirov, R. Pippan, Formation of a W–25% Cu nanocomposite during high pressure torsion, Scripta Mater 52 (2005) 1293–1298.
[44] D. Edwards, I. Sabirov, W. Sigle, R. Pippan, Microstructure and thermostability of a W–Cu nanocomposite produced via high–pressure torsion, Philos. Mag. 92 (2012) 4151–4566.
[45] A.J. Bard, R. Parsons, J. Jordan, Standard Potentials in Aqueous Solutions, Marcel Dekker, New York, 1985.
[46] T. Wada, K. Yubuta, A. Inoue, H. Kato, Dealloying by metallic melt, Mater. Lett. 65 (2011) 1076–1078.
[47] L. Sun, C.L. Chien, P.C. Searson, Fabrication of nanoporous nickel by electrochemical dealloying, Chem. Mater. 16 (2004) 3125–3129.
[48] Y. Gu, C.S. Dong, M.L. Zhong, M.X. Ma, L. Li, W.J. Liu, Fabrication of nanoporous manganese by laser cladding and selective electrochemical de–alloying, Appl. Surf. Sci. 257 (2011) 3211–3215.
[49] T. Chen, Z. Liu, W. Lu, X. Zhou, H. Ma, Fabrication of free–standing nanoporous silver by selectively dissolving gold from gold–silver alloys via a novel converse dealloying method, Electrochem. Commun. 13 (2011) 1086–1089.
[50] K. Wittlich, T. Hirai, J. Compan, N. Klimov, J. Linke, A. Loarte, M. Merola, G. Pintsuk, V. Podkovyrov, L. Singheiser, A. Zhitlukhin, Damage structure in divertor armor materials exposed to multiple iter relevant Elm loads, Fusion Eng. Des 84 (2009) 1982–1986.
[51] T. Hirai, G. Pintsuk, J. Linke, M. Batilliot, Cracking failure study of ITER–reference tungsten grade under single pulse thermal shock loads at elevated temperatures, J. Nucl. Mater. 90–391 (2009) 751–754.
[52] J. Biener, A.M. Hodge, J.R. Hayes, C.A. Volkert, L.A. Zepeda–Ruiz, A.V. Hamza, F.F. Abraham, Size effects on the mechanical behavior of nanoporous au, Nano Lett 6 (2006) 2379–2382.
[53] J. Biener, A.M. Hodge, A.V. Hamza, L.M. Hsiung, J.H. Satcher, Nanoporous Au: a high yield strength material, J. Appl. Phys. 97 (2004) 24301.
[54] Y. Xu, J. Li, L. Liu, Current status and future perspective of recycling copper by hydrometallurgy from waste printed circuit boards, Procedia Environ. Sci. 31 (2016) 162–170.
[55] N. Yoshihara, M. Noda, Chemical etching of copper foils for single-layer graphene growth by chemical vapor deposition, Chem. Phys. Lett. 685 (2017) 40–46.
[56] M.J. Pfeifenberger, M. Mangang, S. Wurster, J. Reiser, A. Hohenwarter, W. Pfleging, D. Kiener, R. Pippan, The use of femtosecond laser ablation as a novel tool for rapid micro-mechanical sample preparation, Mater. Des. 121 (2017) 109–118.
[57] L. Krämer, Y. Champion, K.S. Kormout, V. Maier-Kiener, R. Pippan, Bulk metallic dual phase glasses by severe plastic deformation, Intermetallics 94 (2018) 172–178.
[58] E.W. Andrews, G. Gioux, P. Onck, L.J. Gibson, Size effects in ductile cellular solids. part II: experimental results, Int. J. Mech. Sci. 43 (2001) 701–713.
[59] W.C. Oliver, G.M. Pharr, An improved technique for determining hardness and elastic modulus using load and displacement sensing indentation experiments, J. Mater. Res. 7 (1992) 1564–1583.
[60] W.D. Nix, H. Gao, Indentation size effects in crystalline materials: a law for strain gradient plasticity, J. Mech. Phys. Solids 46 (1998) 411–425.
[61] D. Tabor, The Hardness of Metals, Monographs on the Physics and Chemistry of Materials, OUP Oxford, Oxford (UK), 1951.
[62] M.C. Shaw, T. Sata, The plastic behavior of cellular materials, Int. J. Mech. Sci. 8 (1966) 469–478.
[63] R. Pal, Porosity-dependence of effective mechanical properties of pore-solid composite materials, J. Compos. Mater. 39 (2005) 1147–1158.
[64] T. Ozkan, M.T. Demirkan, K.A. Walsh, T. Karabacak, A.A. Polycarpou, Density modulated nanoporous tungsten thin films and their nanomechanical properties, J. Mater. Res 31 (2016) 2011–2024.
[65] T.J. Balk, C. Eberl, Y. Sun, K.J. Hemker, D.S. Gianola, Tensile and compressive microspecimen testing of bulk nanoporous gold, JOM-US 61 (2009) 26.
[66] J. Erlebacher, M.J. Aziz, A. Karma, N. Dimitrov, K. Sieradzki, Evolution of nanoporosity in dealloying, Nature 410 (2001) 450.
[67] J. Rugolo, J. Erlebacher, K. Sieradzki, Length scales in alloy dissolution and measurement of absolute interfacial free energy, Nat. Mater. 5 (2006) 946.
[68] J.M. Dona, J. Gonzalez-Velasco, Mechanism of surface diffusion of gold adatoms in contact with an electrolytic solution, J. Phys. Chem. 97 (1993) 4714–4719.
[69] K. Oura, M. Katayama, A.V. Zotov, V.G. Lifshits, A.A. Saranin, Surface Science, Advanced Texts in Physics, Springer, Berlin, Heidelberg, 2003.
[70] G. Pia, F. Delogu, Coarsening of nanoporous Au: relationship between structure and mechanical properties, Acta Mater 99 (2015) 29–38.
[71] J. Guo, M.J. Duarte, Y. Zhang, A. Bachmaier, C. Gammer, G. Dehm, R. Pippan, Z. Zhang, Oxygen-mediated deformation and grain refinement in Cu-Fe nanocrystalline alloys, Acta Mater 166 (2019) 281–293.
[72] D. Scheiber, R. Pippan, P. Puschnig, L. Romaner, Ab initiosearch for cohesion-enhancing impurity elements at grain boundaries in molybdenum and tungsten, Modelling Simul. Mater. Sci. Eng. 24 (2016) 85009.
[73] K. Babinsky, J. Weidow, W. Knabl, A. Lorich, H. Leitner, S. Primig, Atom probe study of grain boundary segregation in technically pure molybdenum, Mater. Charact. 87 (2014) 95–103.
[74] L.L.Y. Chang, B.L. Phillips, Phase relations in refractory metal-oxygen systems, J. Am. Ceram. Sco. 52 (1969) 527–533.
[75] R. Restori, D. Schwarzenbach, Charge density in cuprite, Cu2O, Acta Cryst 42 (1986) 201–208.
[76] Z. Pan, L.J. Kecskes, Q. Wei, The nature behind the preferentially embrittling effect of impurities on the ductility of tungsten, Comp. Mater. Sci. 93 (2014) 104–111.
[77] K.R. Mangipudi, E. Epler, C.A. Volkert, Topology-dependent scaling laws for the stiffness and strength of nanoporous gold, Acta Mater 119 (2016) 115–122.
[78] R. Liu, A. Antoniou, A relationship between the geometrical structure of a nanoporous metal foam and its modulus, Acta Mater 61 (2013) 2390–2402.
[79] X. Sun, G. Xu, X. Li, X. Feng, H. Gao, Mechanical properties and scaling laws of nanoporous gold, J. Appl. Phys. 113 (2013) 23505.
[80] M.R. Shankar, A.H. King, How surface stresses lead to size-dependent mechanics of tensile deformation in nanowires, Appl. Phys. Lett. 90 (2007) 141907.
[81] W.X. Zhang, T.J. Wang, Effect of surface energy on the yield strength of nanoporous materials, Appl. Phys. Lett. 90 (2007) 63104.
[82] H.L. Fan, D.N. Fang, Modeling and limits of strength of nanoporous foam, Mater. Design 30 (2009) 1441–1444.
[83] U.K. Vashi, R.W. Armstrong, G.E. Zima, The hardness and grain size of consolidated fine tungsten powder, Metall. Trans. 1 (1970) 1769–1771.
[84] M. Kosmidou, M.J. Detisch, T.L. Maxwell, T.J. Balk, Vacuum thermal dealloying of magnesium-based alloys for fabrication of nanoporous refractory metals, Mrs. Commun. 9 (2019) 144–149.